JOC The Journal of Organic Chemistry

pubs.acs.org/joc Article

Pathway Bifurcations in the Activation of Allylic Halides by Palladium and Their Influence on the Dynamics of η^1 and η^3 Allyl Intermediates

Malkaye Kpante and Lawrence M. Wolf*

Cite This: https://doi.org/10.1021/acs.joc.1c00891 Read Online

ACCESS | Metrics & More | Article Recommendations | SI Supporting Information

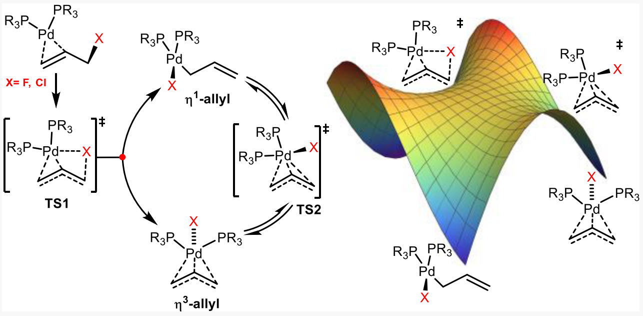

ABSTRACT: Transition-metal-catalyzed allylic substitution often exhibits complex product selectivity patterns, which have been primarily attributed to $\pi \leftrightarrow \sigma \leftrightarrow \pi$ isomerization of the η^1 and η^3 allyl intermediates. Product selectivity may be even further complicated if η^1- and η^3-allyls share a single transition state (TS), leading to their formation resulting in a post-transition-state bifurcation (PTSB). In this work, density functional theory calculations using ab initio molecular dynamics (AIMD) have been carried out that support the presence of a PTSB in Pd-catalyzed allylic halide activation directly influencing product selectivity. The AIMD results initiated from the TS predict the η^1-allyl to be favored in the gas phase and a low dielectric ($\varepsilon < 2.5$) for trialkylphosphines, while the selectivity shifts toward the η^3-allyl in higher dielectrics. The minimum energy path is also predicted to shift in product preference, consistent with the dynamics predictions. The bifurcation in allylic chloride activation is predicted to largely favor the η^3-allyl at any solvent polarity. A PTSB was also discovered to be present in Ni and Pt allylic activation but with less bifurcation. These results offer a unique view into the mechanism of metal-catalyzed allylic substitution.

■ INTRODUCTION

Transition-metal-catalyzed bond activation and subsequent functionalization have revolutionized organic synthesis and method development since its inception. Among the most popular methods are derived from the Tsuji–Trost allylic alkylation reaction involving allylic bond activation on account of the weaker allylic bond strength.[1−4] Critical to the reactivity and selectivity of allylic functionalization is the dynamic nature of the interconversion between the resulting η^3 and η^1 allyl intermediates. However, the intrinsic dynamics of this π-allyl intermediacy has not been explored with respect to the possible presence of post-transition-state bifurcations (PTSBs).[5]

Allylic bond activation is a critical step in metal-catalyzed allylic substitution reactions and can be performed in an asymmetric manner using chiral ligands.[6] Allylic C−H activation is also a key step in alkene isomerization.[7,8] The relatively weak allylic bond strength is responsible for selective allylic functionalization.[9]

The dynamics of allyl intermediates can have a profound effect on the stereoselectivity and the mechanism has been extensively investigated.[10] Allyl complexes can readily isomerize through combinations of $\eta^1-\eta^3-\eta^1$ interconversions (Figure 1). The stereochemistry in the substrate can be partially or entirely degraded as a result of this $\eta^1-\eta^3-\eta^1$ isomerization. Normally, only the η^3-allyl intermediate is considered to be the initial oxidative addition product, which then may isomerize to the η^1-allyl. However, if a PTSB is present, the η^1-allyl could be formed through both direct oxidative addition/insertion or through isomerization from the η^3 allyl. The η^3 and η^1 allyl intermediates would thus share the same transition state.

This investigation aims at determining whether a PTSB is operative in these cases and how product selectivity is determined. For this to occur, a *syn* oxidative addition should be preferred, in which the X leaving group departs on the same face of the allyl bound to the metal. The substrate, metal, ligand, solvent, and the leaving group all determine whether the *syn* or *anti* oxidative addition mode is preferred.[11−13] Nonpolar solvents and weakly donating ligands favor the *syn* pathway, while polar solvents and strongly donating ligands favor the *anti* pathway. In summary, the *anti* path is favored when conditions are conducive to a greater charge being transferred to the leaving group and the opposite is the case for

Received: April 17, 2021

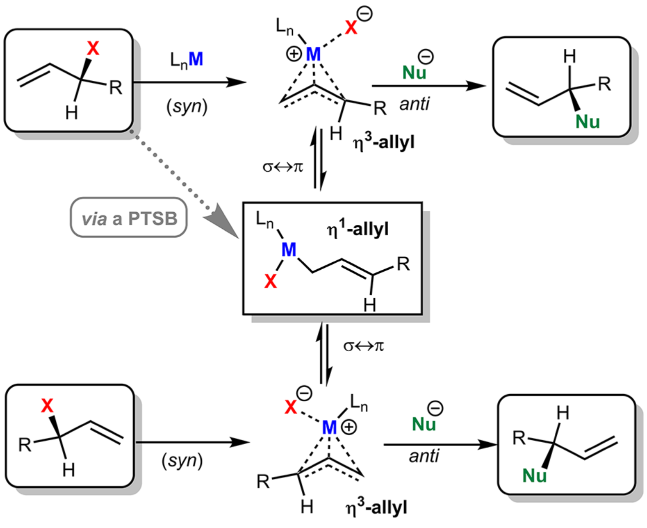

Figure 1. Classical pathways for allyl metal dynamics in black. The gray dashed arrows suggest the formation of the η^1 product directly via a PTSB.

the *syn* path. This investigation is focused on conditions favoring the latter *syn* pathway.

Examples continue to emerge where interconverting intermediates or products share a single transition state for their formation and transition-state theory (TST)[14,15] loses its predictive power.[5,16] These cases are particularly prevalent in pericyclic reactions.[17−42] Examples of PTSBs in transition-metal-catalyzed reactions are more rare, comprising mostly of gold and rhodium carbene intermediates,[43−54] but given the rich and diverse chemistry of organometallic systems, there are likely many more cases yet to be discovered. Furthermore, it is possible that more than two products may share a single transition state, which has been realized in a trifurcated cycloaddition process.[40] Metal-catalyzed cases where a shallow intermediate is dynamically bypassed are also increasingly more common.[54−60] Recently, dynamics effects in the metal-catalyzed 1,4-hydride transfer have been explored in which an intermediate is dynamically bypassed between isomeric π-allyl intermediates.[61]

In these cases, where TST is less predictive, one often must resort to the analysis of molecular dynamics trajectories for obtaining quantitative insight regarding product selectivity. To make matters more challenging, experimental confirmation of such phenomena is either exceptionally challenging or not practically feasible. Since TST cannot be applied in these cases, attempts have been made to predict product distributions by the shape of the potential energy surface (PES)[36] as well as automated routes for their location and making predictions.[62,63] Attempts have also been made to design new reactions that contain PTSBs.[42] Such surfaces with PTSBs have the potential to lead to complex selectivity patterns or even selectivity degradation. A system that often exhibits complex selectivity patterns involves *allyl−metal* intermediates.

Allylic activation by transition metals has been mostly accepted as leading to an η^3-like intermediate. The resulting η^1 and η^3 allyl intermediates undergo interconversion, via $\sigma-\pi$ isomerization, while normally only the η^3-allyl is proposed to exist on the minimum energy path (MEP) connected to the reactant. Our hypotheses from preliminary studies in allylic chloride activation[13] suggests that both η^1 and η^3 allyl intermediates may share a single transition state in these systems (Figure 2). This further complicating perspective has the potential to impact the current mechanistic understanding of metal allyl chemistry if it can be definitively demonstrated.

Fluorine has also been shown to be a competent leaving group in transition-metal-catalyzed allylic functionalization despite its high bond strength to carbon.[64−73] Metal-catalyzed allylic substitution of allylic fluorides was demonstrated using palladium[64] and platinum[65] $M(PPh_3)_4$ complexes. Higher stereochemical integrity of the products was observed under platinum catalysis. Unusual ligand effects and stereochemical leakage were noted on the selectivity. Given the complex inherent dynamics in palladium allyl chemistry, PTSB-created effects will complicate the selectivity even further, particularly in acyclic systems with C−C bond rotations in the η^1-allyl. Under the possibility of a PTSB in allylic chloride activation, allylic fluorides could exhibit similar behavior. Allyl fluorides appeared to be a good candidate for demonstrating the presence of PTSBs in metal-catalyzed allylic activation and was thus also explored computationally.

The aim of this investigation was to determine whether PTSBs are operative in Pd-promoted allylic activation, specifically of C−Cl and C−F bonds in a *syn* manifold (Figure 3), and whether product selectivity could be impacted. The scope of this study includes topological analysis of the potential energy surface, molecular dynamics simulations, and the probing of solvation effects to understand the complex nature

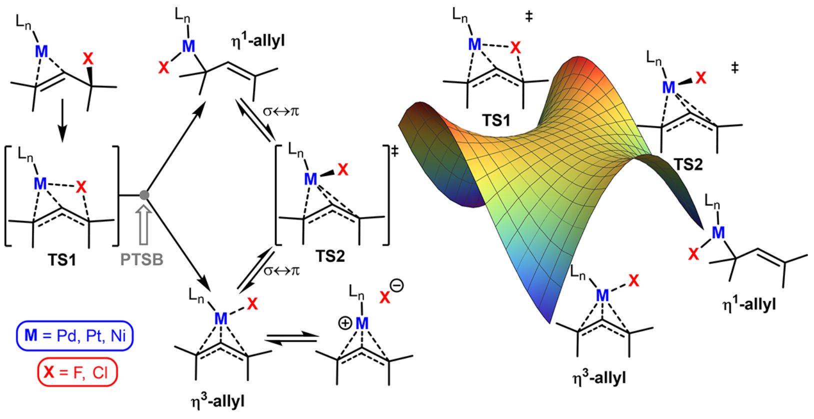

Figure 2. PTSBs in allylic bond activation forming both η^1- and η^3-allyl products with a hypothetical bifurcating potential energy surface displayed to the right.

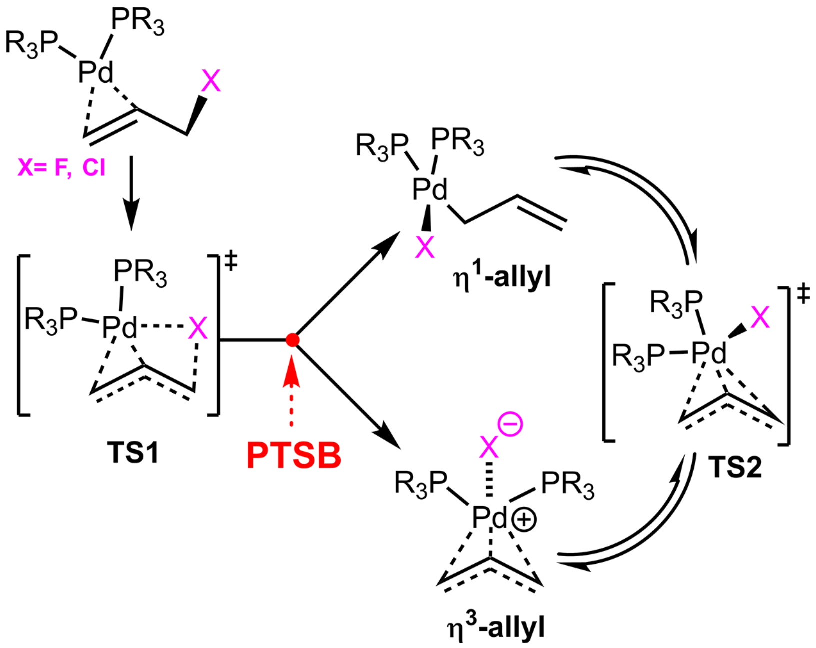

Figure 3. Proposed PTSBs in Pd-catalyzed allylic activation with X = F, Cl.

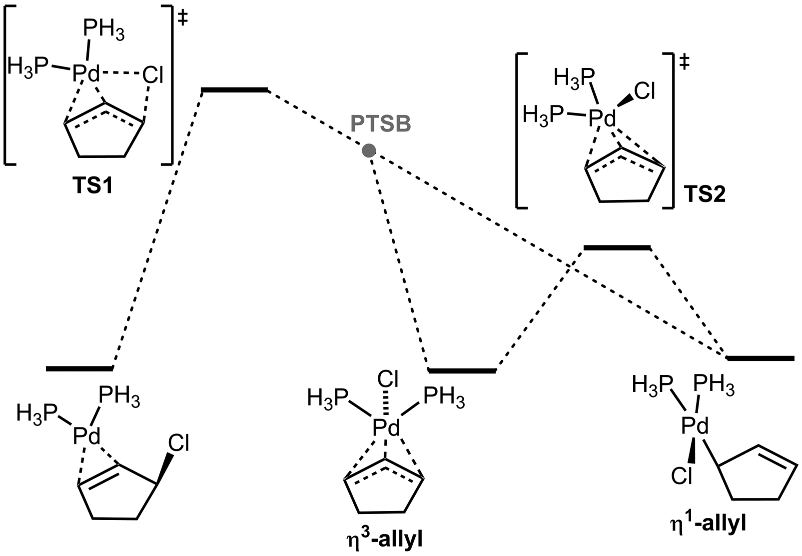

Figure 4. Reaction energy profile reported for allylic chloride activation.[13]

of this system. The results could have broader implications in metal-catalyzed allylic activation involving π-allyl intermediates.

■ COMPUTATIONAL METHODS

All geometry optimizations were performed using the hybrid density functional B3LYP[74,75] augmented by the D3 dispersion correction with BJ-damping (B3LYP-D3).[76] The B3LYP functional generally performs satisfactorily for describing palladium-promoted bond activation processes from benchmark studies.[77] The def2-SVPD[78−80] basis set was used for geometry optimizations and energies reported in reaction energy profiles were obtained at the def2-TZVPPD level on the def2-SVPD-optimized geometries. The 28 inner-shell core electrons of the palladium atom were described by the def2 effective core potential and account for scalar relativistic effects (def2-ecp). The resolution-of-identity (RI) approximation[81,82] was applied using auxiliary basis sets to approximate the Coulomb potentials. The COSMO model[83,84] was used for modeling implicit solvation. Stationary points were characterized by evaluating the harmonic vibrational frequencies at the optimized geometries. Zero-point vibrational energies (ZPVE) were computed from the corresponding harmonic vibrational frequencies with a scaling factor of 0.99. The relative free energies (ΔG) were determined at standard pressure (1 bar) and at the reaction temperature of 298 K. The thermal and entropic contributions were evaluated within the rigid-rotor harmonic-oscillator approximation. Ab initio molecular dynamics (AIMD) simulations were performed using the Frog module within Turbomole. All trajectories were initiated at a temperature of 300 K with atoms being assigned randomized velocities using randomized input seed numbers distributed using a Gaussian distribution with a temperature-dependent variance and propagated classically using the Verlet leapfrog algorithm for transforming the gradients into new positions and velocities. The trajectory step size was set to 0.5 fs with a total of 500 steps for the total lifetime of most productive trajectories. Intrinsic reaction coordinate (IRC) calculations were used to ensure that transition-

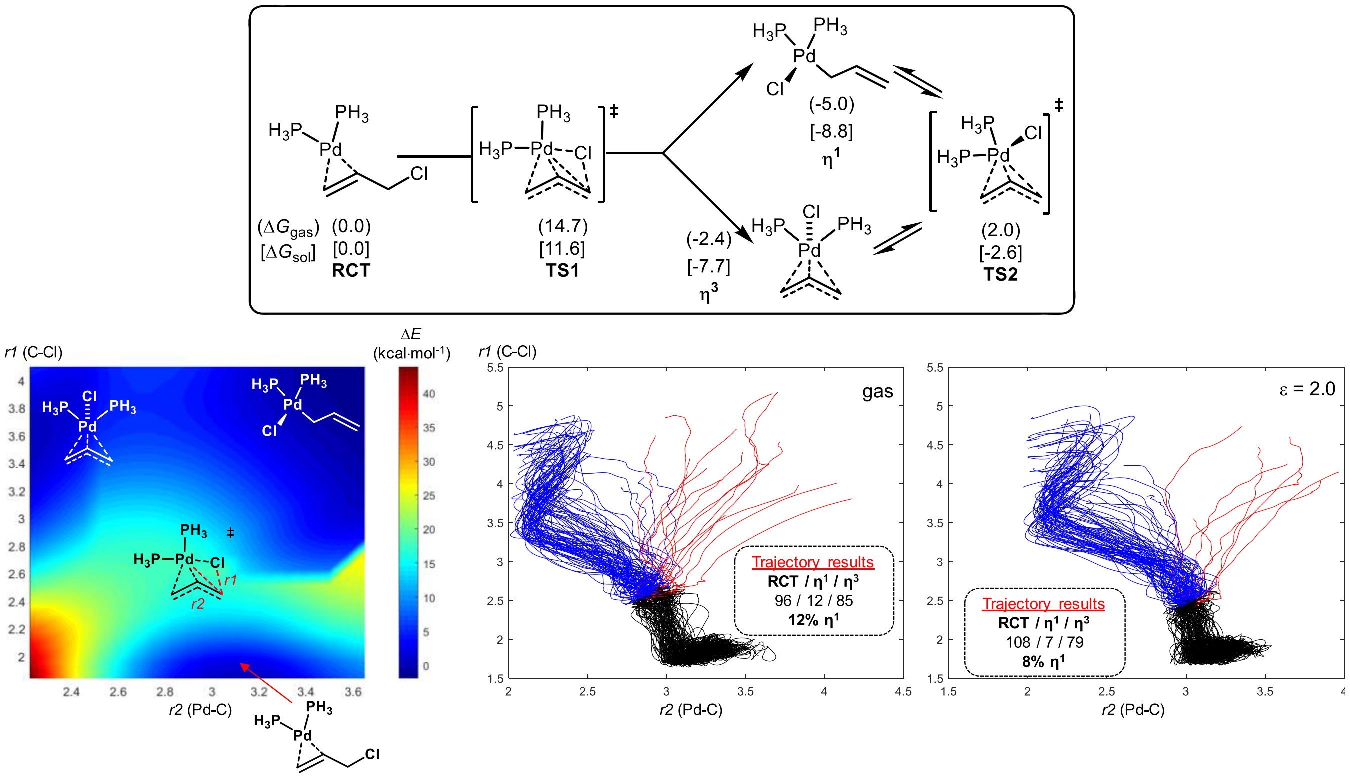

Figure 5. (a) Mechanism for activation of allyl chloride using Pd(PH_3)$_2$ with Gibbs free energies in the gas phase and solvent with $\varepsilon = 2.0$ obtained at the B3LYP-D3/def2-TZVPPD//B3LYP-D3/def2-SVPD level. (b) PES constructed from a double relaxed scan of the Pd−C and C−Cl bond lengths. (c) Plots of ca. 100 product and ca. 100 reactant trajectories for allylic chloride activation using L = PH_3 performed in the gas phase (middle) and with dielectric $\varepsilon = 2.0$ (right).

state structures (confirmed by frequency analysis) led to the assumed reactants and products and for locating the minimum energy path. The criterion used for determining the identity of the product of a trajectory was the Pd−C bond distance, where the carbon is bonded to the halogen (fluorine or chlorine). A trajectory is defined as leading to the η^1-allyl if d(Pd−C) > 3.2 Å and to the η^3-allyl if d(Pd−C) < 2.5 Å. Additional functionals including PBE0,[85−88] M06-L,[89] TPSS,[90] and TPSSh,[91] with and without a dispersion correction in some cases, were also explored to confirm whether the bifurcations were qualitatively general spanning a selection of functionals, which included minimum energy path (MEP) and MD analyses in both the gas and solution phases. DLPNO-CCSD(T)[92−94] single-point energy calculations were performed on the B3LYP-D3-optimized geometries for the purpose of method validation using ORCA 4.2.1.[95,96] Relaxed potential energy scans (PESs) were performed across either the C−F or C−Cl bond-breaking and Pd−C bond-forming coordinates. NCIPLOT[97] was used for constructing non-covalent interaction (NCI) isosurfaces for highlighting the developing van der Waals contacts between the ionizing fluoride and the ligands to varying extents. Distances are given in angstroms (Å), and angles are in degrees (°). 3D renderings of stationary points were generated using CYLview 1.0.[98] All calculations were performed using Turbomole v7.3.1.[99,100]

■ RESULTS AND DISCUSSION

Allylic Chloride Activation. Previous computational investigations into Pd-catalyzed allylic chloride activation had supported the presence of a PTSB in cases when the Pd atom adds in a *syn* fashion with the leaving group but was neither unambiguously demonstrated using molecular dynamics nor through a detailed exploration of the potential energy surface, which are both necessary for confirming the presence of PTSBs (Figure 4).[13] The conclusion was based on careful inspection on the relation between the forming and breaking bonds included in both η^1 and η^3 intermediates and the TS leading to their formation. Thus, AIMD simulations were performed here to determine whether the presence of a PTSB was indeed plausible in the activation of an unsubstituted allyl chloride.

The mechanism for activation of allyl chloride by palladium was investigated in both the gas and solution phases. In solvent, the activation energy is lowered and the energetic preference shifts in the direction of the η^3 allyl consistent with η^3 being more polar than η^1. The PES was then constructed by scanning both the C−Cl breaking and Pd−C (α to Cl) forming bonds using the PH_3 ligand at the B3LYP-D3/def2-SVPD level in the gas phase (Figure 5). While PH_3 is not necessarily an accurate experimental ligand probe, the results provide insight into whether the pursuit of larger, more experimentally viable ligands would be worthwhile. The gas-phase PES demonstrates that a bifurcation is likely present by scanning the relevant bond-forming and -breaking coordinates with the minimum energy path (MEP) leading to the η^3 intermediate. From the region of **TS1**, there are diverging descending channels leading to both of the blue, low-energy wells occupied by η^1 and η^3 allyls, which interconvert via **TS2**, which is located at r_1(C−F) = 3.8 Å and r_2(Pd−C) = 2.7 Å. According to the MD simulations, 88% of the product trajectories lead to the η^3 product and 12% lead to the η^1 product. Approximately, 50% of the overall trajectories lead to the expected reactant. These results also support the presence of a PTSB. The branching however is minor, and outside of the gas phase in the presence of a low dielectric ($\varepsilon = 2.0$), nearly 92% product trajectories lead to the η^3 allyl. Given the high selectivity for η^3 in both the gas and solution phases, this

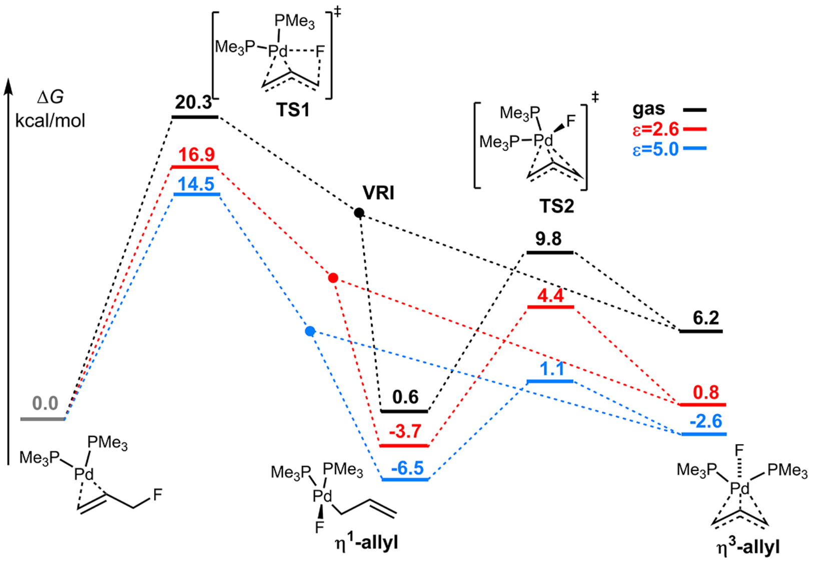

Figure 6. Reaction Gibbs energy profiles for allylic fluoride activation in the gas phase, ε = 2.6 and 5.0, with the PMe_3 ligand determined at the B3LYP-D3/def2-TZVPPD//B3LYP-D3/def2-SVPD level.

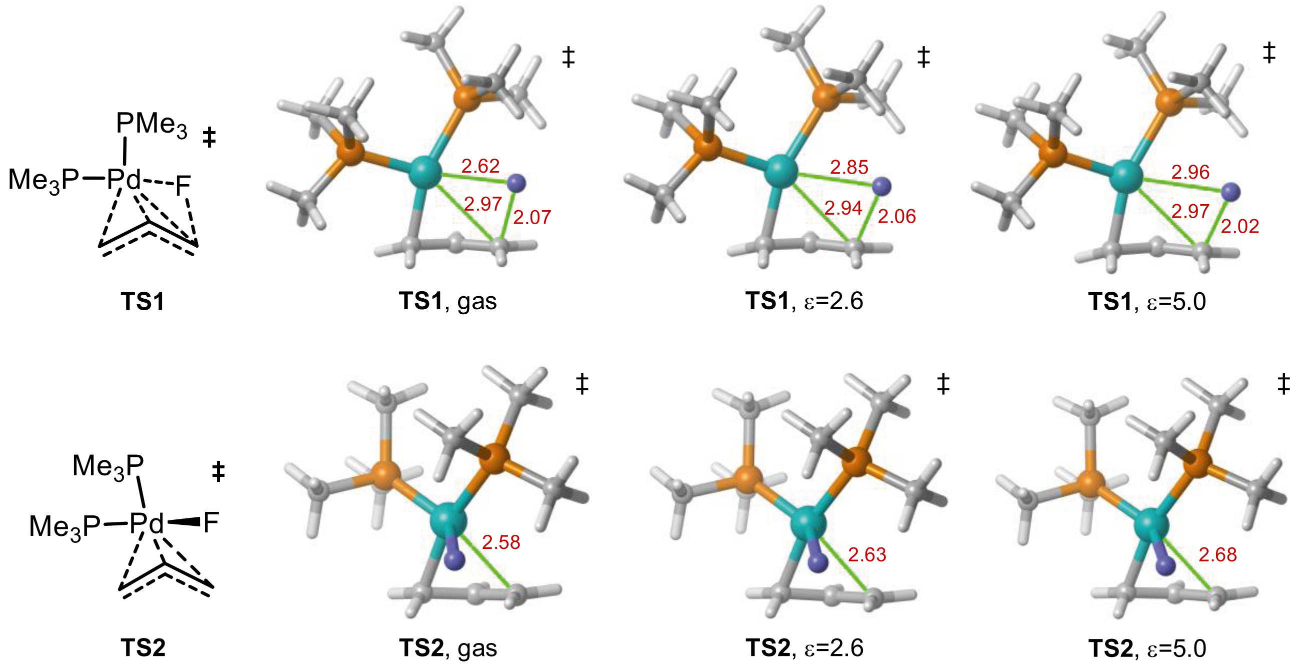

TS1 **TS1**, gas **TS1**, ε=2.6 **TS1**, ε=5.0

TS2 **TS2**, gas **TS2**, ε=2.6 **TS2**, ε=5.0

Figure 7. Transition-state structures for **TS1** and **TS2** at varying dielectrics with the PMe_3 ligand.

bifurcation may not have a great consequence from a synthetic standpoint. Since the Pd−Cl bond in the η^3 form is largely ionic, the ionizing ability of the halogen should in principle influence the selectivity favoring η^3. Fluoride is a leaving group with much poorer ionizing ability indicating possibly a less preference for η^3 over η^1 and was thus pursued further as a system with greater potential for exhibiting dynamics-related effects over allyl chloride.

Allylic Fluoride Activation. The reaction profiles for allylic fluoride activation were investigated using PH_3, PMe_3, and PPh_3 as ligands. The corresponding profiles using PMe_3 are shown here (Figure 6). The point after the TS where the paths bifurcate is defined as the valley-ridge inflection (VRI) point. The other ligand profiles are available in the Supporting Information. The choice of dielectric constants was based on the MEP path switching, as determined from the IRC calculations discussed separately. The inclusion of solvation induces a shift in the profile toward lower energy for all points relative to the reactant. The path connecting η^1 to η^3 via TS2 was confirmed by inspection of the IRC. The Pd−F bond in the η^3-allyl is intermediate between covalent and ionic, with η^3 being closer to covalent in lower dielectric and a coupled ion pair in higher dielectric media (Figure S17). The Pd−F bond is more polarized in both η^1 and η^3 intermediates than the reactant C−F bond, causing a dielectric-dependent thermodynamic shift. A particularly noteworthy change with increasing dielectric is in the η^1 and η^3 energetic preference. The η^1 allyl is preferred in each dielectric, but its preference is diminished with increasing dielectric; $\Delta G_{\eta^3-\eta^1}$ = 5.6, 4.5, and 3.9 kcal·mol^{-1} at ε = gas, 2.6, and 5.0, respectively. This

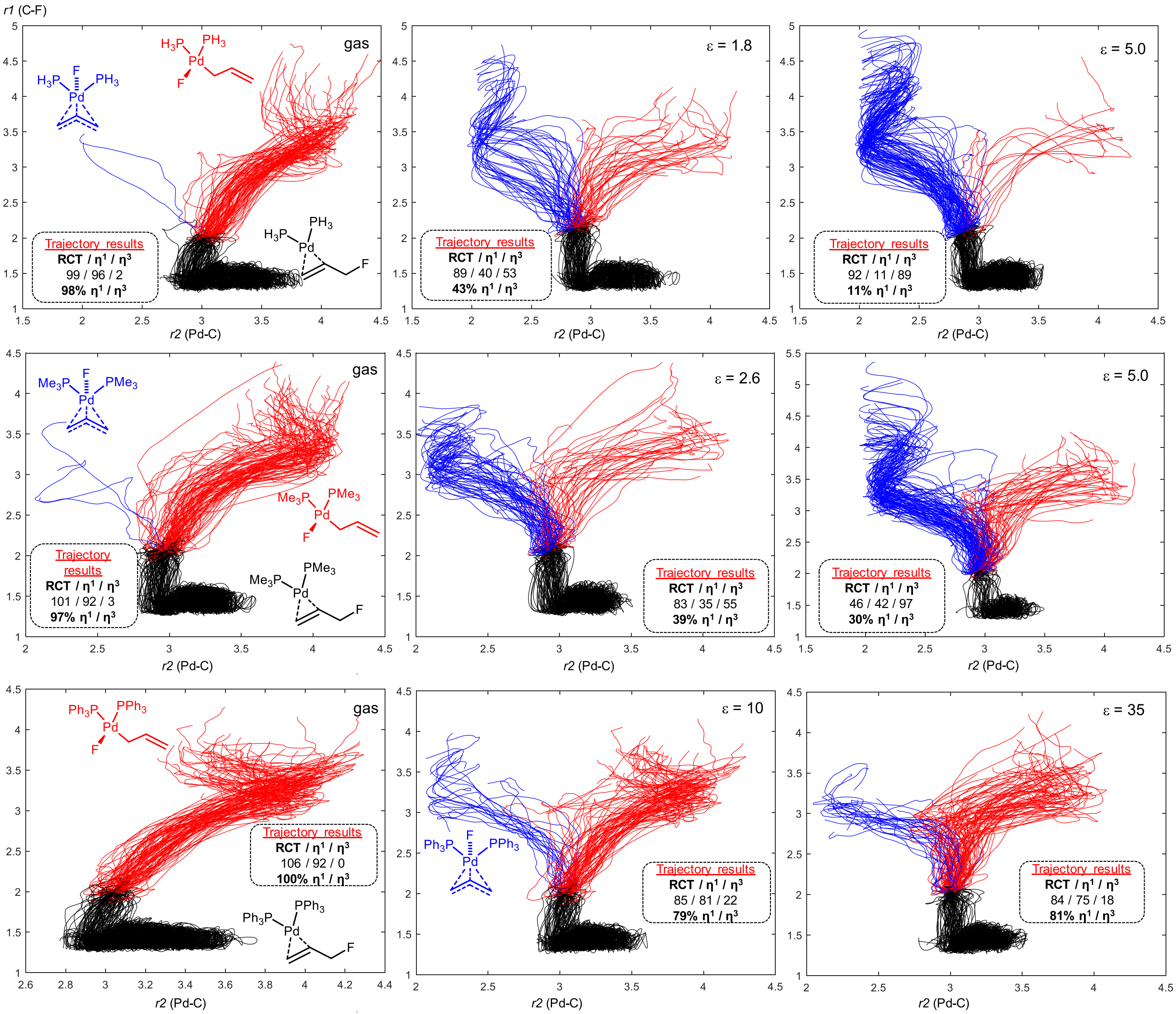

Figure 8. Plots of ca. 100 product and ca. 100 reactant trajectories for allylic fluoride activation using (top) L = PH_3, (middle) L = PMe_3, and (bottom) L = PPh_3 performed in the gas phase and with varying dielectric constants, ε (COSMO), at the B3LYP-D3/def2-SVPD level. Each axis is in units of Å.

thermodynamic Hammond shift causes the position of **TS2** to shift in the direction of the η^1 allyl as determined by inspection of the **TS2** geometries, which may influence possible dynamic preferences.

Using the ligands discussed here, the *syn* pathway is predicted to be preferred over the *anti* pathway at $\varepsilon \leq 2.5$ (Figure S22).[13] The use of different substrates and more π-acidic ligands would broaden the dielectric range where the *syn* manifold would be operable.

Inspection of the structures for transition states **TS1** and **TS2** reveals interesting dielectric-dependent trends. The position of **TS1** appears slightly earlier with increasing dielectric as determined by the increasing Pd−F bond length and to some extent the C−F bond length, consistent with the energetic shifts (Figure 7). The Pd−C bond remains relatively constant, which is a major coordinate connecting η^1 and η^3. In **TS2**, the same Pd−C bond elongates with increasing dielectric, shifting toward the η^1 product, consistent with the Hammond predictions from the energetic shifts. In summary, increasing dielectric shifts **TS1** slightly toward the reactant side, while **TS2** is shifted toward the η^1 allyl intermediate. These considerations will be important for rationalizing the MD results that follow.

A PTSB in allylic fluoride activation was explored by inspecting the PESs and by analysis of the dynamics (Figure 8). The dynamics was performed in a similar fashion as in the chloride case while exploring the ligands PH_3, PMe_3, and PPh_3. In stark contrast to the chloride case, the η^1 product is favored over the η^3 product as 98% of productive trajectories led to η^1 in the gas phase for PH_3 and 97% for PMe_3. Dissociating fluoride requires charge stabilization, which is obtained through the developing Pd interaction leading to η^1-allyl. As a dielectric is introduced, the trajectory distribution shifts in the direction of the η^3-allyl. Intriguingly, as the dielectric of the medium is increased further to 5.0, a more profound shift in preference for the η^3-allyl is manifested. IRC calculations are consistent with this preference switch as the product of the MEP agrees with the dynamics preference. The MEP switching

https://doi.org/10.1021/acs.joc.1c00891
J. Org. Chem. XXXX, XXX, XXX−XXX

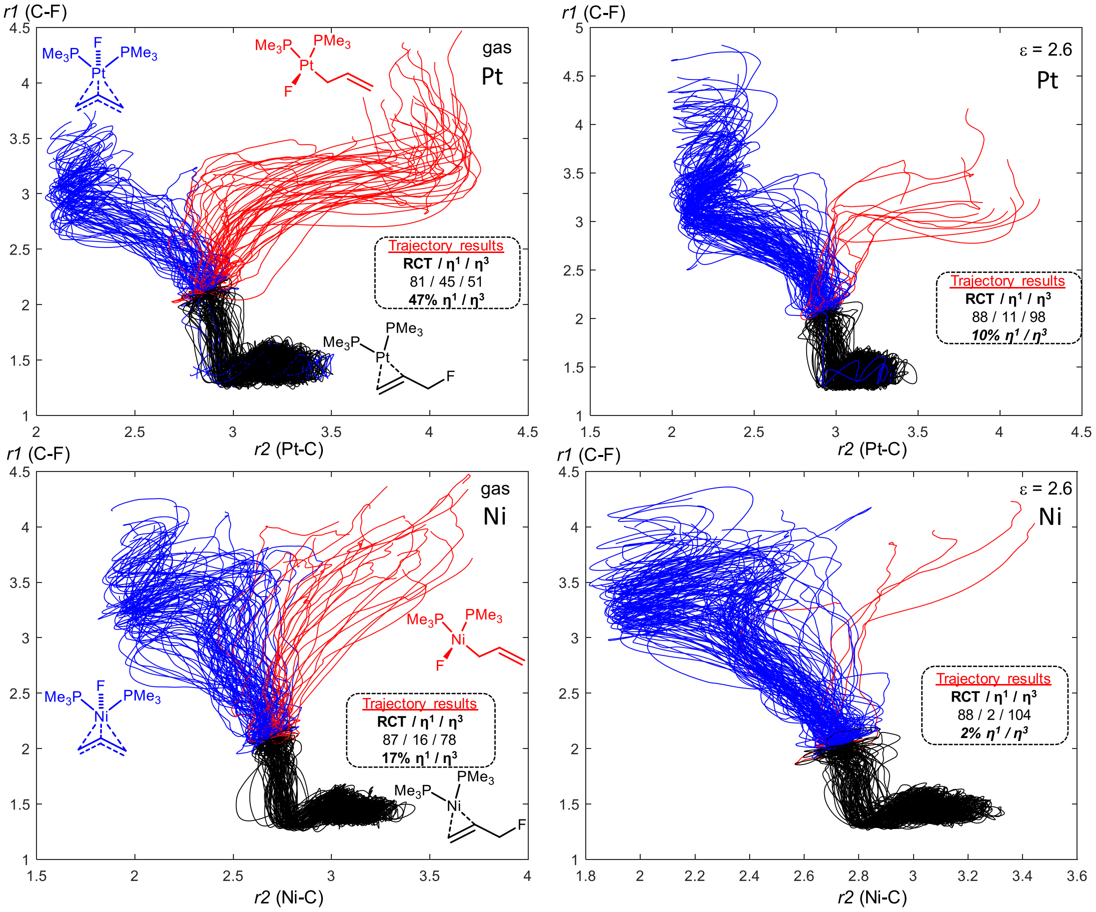

Figure 9. Plots of ca. 100 product trajectories and ca. 100 reactant trajectories for allylic fluoride activation using Pt$(PMe_3)_2$ (top) and Ni$(PMe_3)_2$ (bottom) performed in the gas phase and at ε = 2.6 (COSMO) at the B3LYP-D3/def2-SVPD level.

point as determined from the IRC calculations was located at a dielectric of ~1.8 for PH_3 and ~2.6 (e.g., benzene or toluene) for PMe_3. According to our understanding, this would be a rare example of a solvation-dependent minimum energy path in a reaction with a PTSB.[34] Furthermore, the changing dielectric causes **TS1** to appear earlier while remaining unchanged along the **TS2** Pd−C coordinate. Solvation only appears to affect the relative positions of **TS1** and **TS2**, and it could thus be a convenient handle for exploring product ratios while keeping **TS1** relatively constant with respect to a changing **TS2**, on the basis of the Hammond postulate.

The predicted branching ratios do exhibit some dependence on the density functional. Additional functionals that perform reasonably well for Pd-promoted bond activation[77] including PBE0-D3, M06-L, TPSSh-D3, and TPSS-D3 were also used to perform the MD simulations in both the gas phase and in a dielectric of ε = 2.6 using the PMe_3 ligand to examine the generality of the bifurcation (Table S1). In the gas phase, all functionals predict >90% preference for the η^1-allyl excluding PBE0. In using PBE0, the preference is dependent on whether a dispersion correction is included with PBE0-D3 predicting 33% η^1 and PBE0 predicting 78% η^1. Benchmark studies indicated that the D3 correction with PBE0 resulted in no improvement in the mean absolute deviations in the energies with respect to kinetics and only a small improvement (ca. 0.3 kcal·mol^{-1}) in the thermodynamics, so the importance of the D3 correction is inconclusive. For B3LYP, the results do not change in the gas phase with ε = 2.6 or with and without D3. The MGGA functional M06-L predicts the greatest preference for η^1 with 96% η^1 in the gas phase and 57% η^1 with ε = 2.6. TPSSh-D3 gives similar predictions as B3LYP. While the precise branching ratios are subject to variability using DFT, the qualitative conclusion for the existence of a PTSB still holds with the presence of a solvent-dependent product preference switching point being likely.

In contrast, the PPh_3 ligand does not exhibit as strong solvation effects, but a bifurcation is still clearly present. Similar to the smaller ligands, only η^1 formed in the gas phase. As solvation is introduced, η^3 begins to appear. A clear distinction with the PPh_3 case is that there is no product preference switching point as was observed for PH_3 and PMe_3. The product ratios level off to approximately 80% η^1 product selectivity. Clearly, there is a strong preference for the η^1 product with the PPh_3 ligand. It appears that the steric effects of the ligand prevent a peripheral phenyl group from proceeding in close proximity to the α-carbon (C−F), as the η^3 product is generally more sterically encumbered than the η^1 product. The aryl groups may also provide a stabilizing pocket for the dissociating fluoride, preventing significant ionization required for η^3 allyl formation. This preference for η^1 with PPh_3 is in spite of the slight thermodynamic preference for η^3 at higher dielectrics, highlighting a disagreement between the dynamically preferred and thermodynamically preferred products (Figure S20).

At higher dielectrics, the *anti* pathway is predicted to be favored over the *syn* pathway (ε > 2.5) using PPh_3 (Table

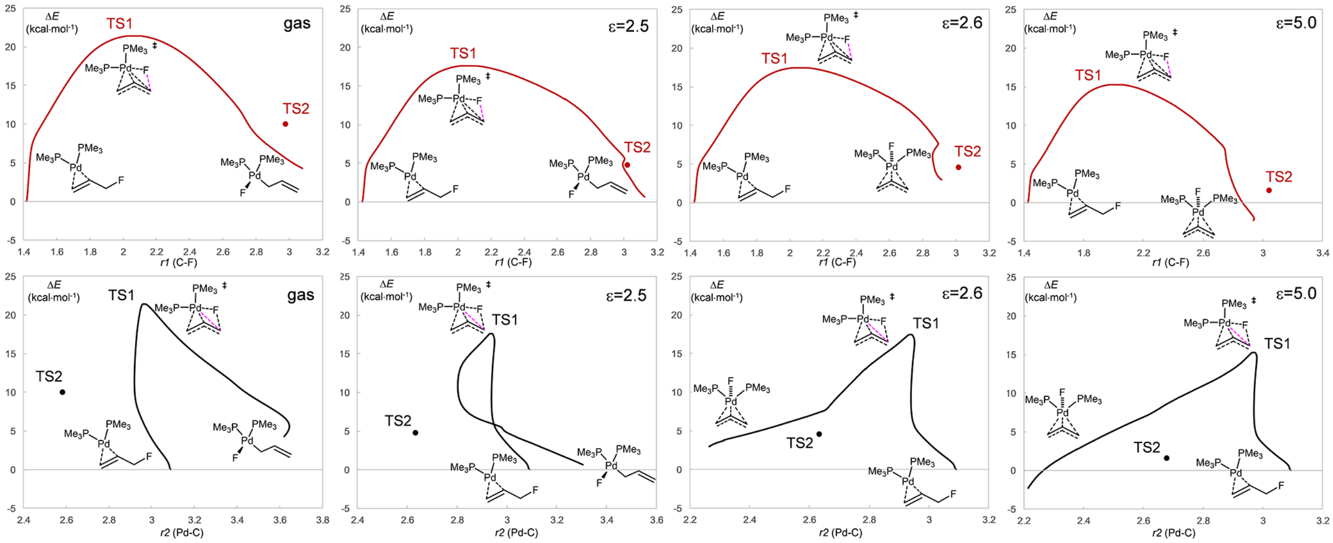

Figure 10. MEPs at varying dielectrics projected along the C−F (top, red) and Pd−C (bottom, black) coordinates using the PMe$_3$ ligand. The relevant bond coordinate is highlighted (magenta) in the corresponding TS1 structures.

S21). At a dielectric of $\varepsilon = 2.0$, B3LYP-D3 predicts >99:1% η^1. The PBE0-D3 method, which appears to be biased toward the dynamics preference for η^3 at lower dielectrics using PMe$_3$, also predicts >99:1 for η^1 at $\varepsilon = 2.0$. Therefore, within the dielectric range of $2.0 < \varepsilon < 10.0$, there is a point where the bifurcation begins to set in.

Allylic Fluoride Activation Using Ni and Pt. In an effort to determine whether this bifurcation was unique to Pd, other metals in Group 10 were also explored for possible PTSB-related effects (Figure 9). Allylic substitution using allylic fluorides with Pt(PPh$_3$)$_4$ has also been demonstrated experimentally.[65] The Pt-catalyzed substitution generally proceeds with higher selectivity than in Pd-catalyzed substitution. Dynamics simulations were carried out on Pt(PMe$_3$)$_2$(allyl)F to gauge how the metal influences the selectivity. While Pt normally favors the *anti* pathway in nonpolar and polar media, the *syn* path could in principle be biased under the appropriate combination of the solvent, ligand, and substrate. Ni(PMe$_3$)$_2$(allyl)F was also investigated for comparison. The dynamics results for Pt indicate that 53% of the product trajectories lead to η^3 in the gas phase (Figure 9). These results are quite different from the Pd case where the vast majority of trajectories led to η^1. The η^3 preference is predicted to dominate in nonpolar media, in contrast to the Pd case (Figure 8). For Ni-catalyzed activation, the dynamics reveals that 83% of the product trajectories lead to η^3 allyl. It may be the case that the less diffuse 3d orbitals of Ni engage in poorer overlap with the departing fluoride required for η^1 formation. Ni also being less electron rich will disfavor partial ionization in the η^3 path. Ni should favor the *syn* pathway over a wider dielectric range than either Pd or Pt being less electron rich. Even more significant dynamics-related effects are thus expected under Ni-catalyzed allylic substitution using triarylphosphine ligands given the stronger preference for *syn* stereochemistry.

Minimum Energy Path Analysis. Inspection of the MEP as a function of the C−F and Pd−C bonds reveals some insights into the nature of the solvation dependence (Figure 10). The MEPs using PMe$_3$ as the ligand with changing dielectric are given. In the gas phase, the C−F bond initially undergoes little change with energy until an energy of $\Delta E = 7$ kcal·mol^{-1} is reached after which a normal, unperturbed transition to the η^1 product is established. The Pd−C bond decreases as the energy increases from 0 to ∼9 kcal·mol^{-1}, which then increases slightly to the TS after which a steep decrease to the product occurs. From **TS1**, the path proceeds in the opposite direction of **TS2** toward the η^1 allyl. With increasing solvation, the profiles are shifted lower in energy. As the dielectric is increased to $\varepsilon = 2.5$, the MEP along the C−F coordinate approaches closer to **TS2** before making a sharp adjustment to avoid the slope upward in energy toward **TS2**. Interestingly, along the Pd−C coordinate at $\varepsilon = 2.5$, the path reaches **TS1** from the reactant in a similar fashion as in the gas phase but changes directions toward the η^3 allyl at ca. 2.8 Å by decreasing the Pd−C bond length. The path then drastically changes course toward the η^1 allyl, as in the gas phase, thus avoiding **TS2**. Presumably, this would represent the region in the vicinity of the VRI point, which is supported by the substantial change with only a slight increase in the dielectric constant from 2.5 to 2.6. Increasing the dielectric ε by only 0.1 to 2.6, the dynamics results predict a change in the product preference from η^1 to η^3, which is reflected in some notable alterations to the C−F and Pd−C energy profiles, and the MEP also leads now to the η^3 allyl. The C−F profile follows a similar path to that from the gas phase and $\varepsilon = 2.5$ through **TS1** until at ca. 2.9Å, 8 kcal·mol^{-1}, after which there is a sharp decrease followed by an increase to the η^3 allyl. The Pd−C profile also follows a similar path as the prior two paths until **TS1** is reached and the bond continues to decrease to the η^3 allyl. At ca. 8 kcal·mol^{-1}, a break in the slope of Pd−C decrease appears, the same energy as in the C−F coordinate, as the path approaches **TS2**. This point again is likely where the MEP begins to approach the VRI region and veers toward the η^3 channel. At a dielectric of $\varepsilon = 5$, the MEP leads to the η^3 product. The analogous breaks in the profiles are less pronounced after the TS as compared with the clear breaks with dielectrics of 2.5 and 2.6. The diminishing break likely suggests that the MEP veers more toward the η^3 channel further from the region of the VRI point, resulting in most of the trajectories leading to η^3.

The solvation dependence on the trajectories is intriguing, particularly in combination with the switch in the MEP

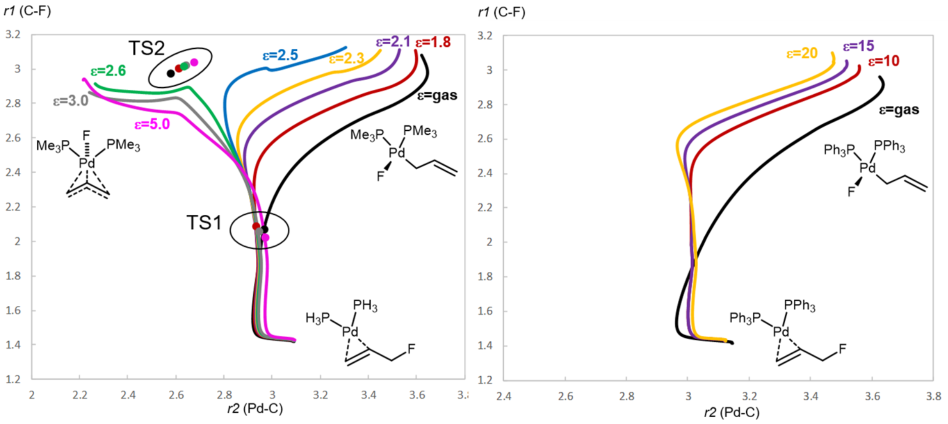

Figure 11. MEPs plotted at varying dielectrics for PMe_3 (left) and PPh_3 (right) ligands. The paths increase in the dielectric constant from right to left.

preference. Solvation dependencies have been noted previously in reactions with PTSBs[34,39] but not in an organometallic process. This switch in MEP product preference strongly suggests the presence of a PTSB independent of the MD results. Inspection of the MEPs in solvent reveals interesting trends, which are more apparent through inspection of the MEPs plotted together (Figure 11). With increasing the dielectric, the position of **TS1** undergoes little change along both the C−F and Pd−C bond coordinates. More influential on the selectivity is the shift in the location of **TS2** with increasing solvation in the direction of the η^1 allyl on account of stabilization of the η^3 allyl. As **TS2** is pulled in the direction of the η^1, the η^3 reaction channel becomes increasingly preferred. In the gas phase, **TS2** is closest to the η^3 allyl, while the path in the highest dielectric (ε = 5.0) is closest to the η^1 allyl. It is clear that the VRI point is in between where the paths of ε = 2.5 and 2.6 veer toward the η^1 and η^3 allyls, respectively. The shift never takes place in cases where the PPh_3 ligand is used. In the gas phase, the Pd−C bond increases more rapidly with changing C−F bond length leading toward η^1 allyl using PPh_3 as compared to PMe_3, demonstrating a stronger pull toward η^3 even in the gas phase using PPh_3.

Some level of understanding of why the use of PPh_3 does not lead to a MEP switch with greater dielectric can be obtained upon inspection of the van der Waals (vdW) contacts between the dissociating fluoride and the CH arene bonds of a PPh_3 ligand using a noncovalent interaction (NCI) analysis (Figure 12). The η^1 path does not involve substantial vdW contacts between the phenyl C−H bonds and the dissociating fluoride, whereas the η^3 path requires tilting of the ligand phenyl groups toward the fluoride bearing carbon with a concomitant shift of the fluoride toward the center of the allyl group to associate with the Pd center. This is a sterically demanding process, which the majority of trajectories avoid. **TS1** already includes contacts between the fluoride with the arenes and would require more substantial contacts should it access the η^3 channel. This vdW contact in **TS1** with PMe_3 C−H bonds is reduced from being more distal and does not inhibit Pd−C bond formation with fluoride migration toward the center of the allyl group to the same extent as with PPh_3. In the greater dielectric, the fluoride can depart further from the substrate using PPh_3, which permits the phenyl groups to adopt the position required for η^3 allyl formation in at least 20% of the trajectories. Additionally, the ligand arene C−H bonds proximal to the ionizing fluoride appear to interact with the fluoride electrostatically inhibiting the requisite degree of dissociation for permitting Pd−C bond formation leading to the η^3 allyl. Successful η^3 trajectories at a dielectric of ε = 10.0 exhibit substantial C−F bond dissociation. Thus, there appears to be to some extent a competition between the arene C−H bonds and solvent in stabilizing the developing charge on the fluoride.

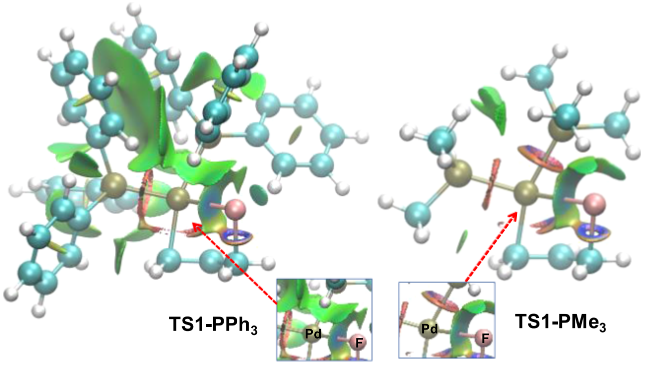

Figure 12. NCI isosurfaces for **TS1**-PPh_3 and **TS1**-PMe_3 highlighting the developing van der Waals contacts between the ionizing fluoride and the ligands to varying extent.

Overlaying the MEPs on the relevant PES with the appropriate dielectric constant provides some insights into the switching preference with the PMe_3 ligand (Figure 13). The MEP in the gas phase is directed along the η^1 channel. With solvation, **TS2** is lowered in energy relative to **TS1** ($\Delta E_{TS1-TS2}$ = 11.4, 12.6, 13.7 kcal·mol^{-1} for ε = gas, 2.6, 5.0, respectively) and is shifted toward the η^1 allyl. Both alterations have the effect of redirecting the MEP toward the η^3 channel. At ε = 2.6, the MEP clearly approaches closely toward **TS2** after which it nearly accesses the $\eta^1 \leftrightarrow \eta^3$ reaction coordinate. These changes in the relative positions of **TS1** and **TS2** contribute to shifting the MEP towards η^3 with increasing solvent dielectric.

Summary and Proposed PTSB Verification. The results in this investigation lend support for the presence of PTSBs as applied to metal-catalyzed allylic activation of C−F and C−Cl bonds but with less bifurcation with C−Cl bonds. The consequences on selectivity may be profound in cases where η^1 and η^3 are formed in comparable amounts. A selectivity-solvent dependence was discovered for activation of allyl fluoride (Figure 14). Intriguingly, the MEP was found to be solvent-

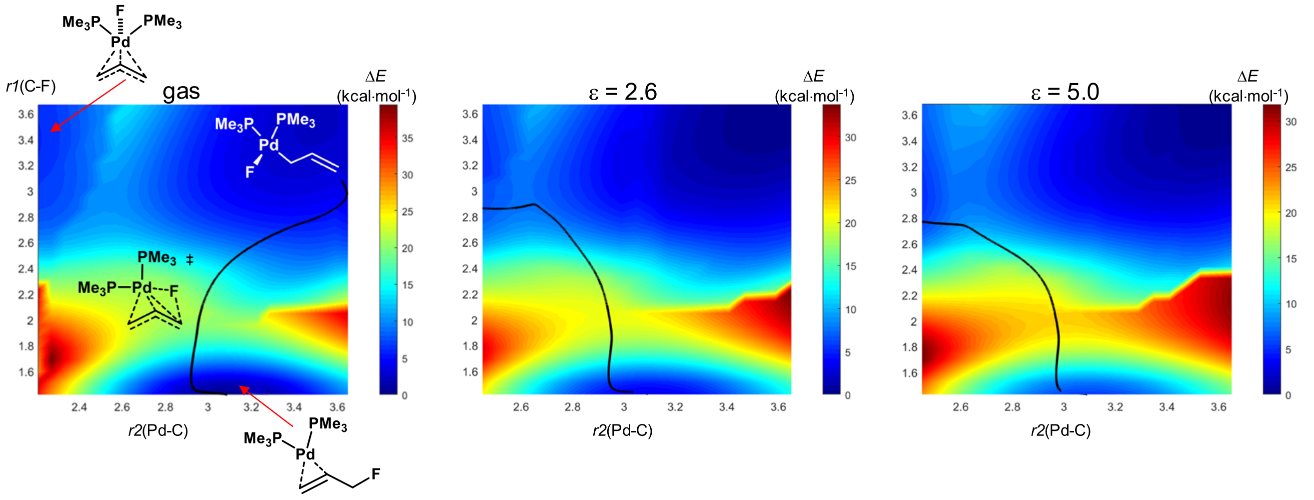

Figure 13. Potential energy contour maps constructed at varying dielectric constants with the MEP overlaid for the PMe_3 ligand determined at the B3LYP-D3/def2-SVPD level.

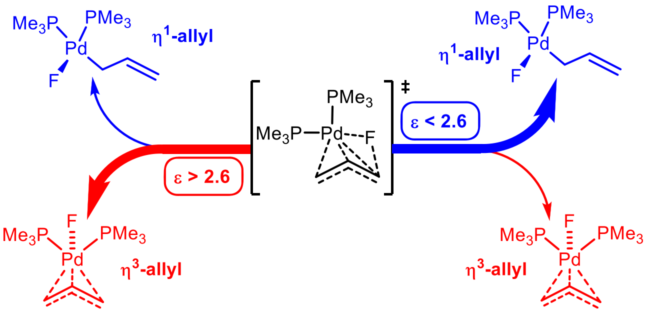

Figure 14. Summary of the MEP switching point at $\varepsilon = 2.6$ using the PMe_3 ligand.

dependent, which is without precedent on a bifurcating PES. The $\sigma \leftrightarrow \pi$ isomerization is often used to explain the loss in stereochemical integrity starting from substrates with a defined stereochemistry of either the alkene geometry or the configuration of the activated carbon, which is shown here to be compounded by initial formation of both allyl intermediates via a PTSB.

Confirming the presence of PTSBs experimentally can be particularly challenging, especially if the bifurcating step is prior to the product selectivity determining step, which is usually nucleophilic addition to the η^3-allyl, as may be the case here. Experimentally, allylic fluoride activation and subsequent substitution have been achieved and the mechanism was investigated using PPh_3 as the ligand with cyclic substrates.[64] A stereochemical probe, which is affected by the $\eta^3(1) \leftrightarrow \eta^1 \leftrightarrow \eta^3(2)$ isomerization, could in principle be used to support the presence of a PTSB. An example of a labeling strategy for PTSB verification is provided (Figure 15). A diastereomerically defined alkene with a deuterium label could be used as the substrate in nonpolar solvent. The η^3-allyl is usually the expected initial product without considering a bifurcation. Supposing the rate of nucleophilic attack in the second step is much greater than the rate of isomerization to the η^1-allyl ($k_2 \gg k_1$), then products ***cis*-A** and **B** would be predicted to be the only observable products in nearly equal amounts, including secondary isotopic effects, which is likely an achievable condition given the predicted barrier for interconversion through k_1 is predicted to be ca. 9 kcal·mol^{-1} (Figure S20).

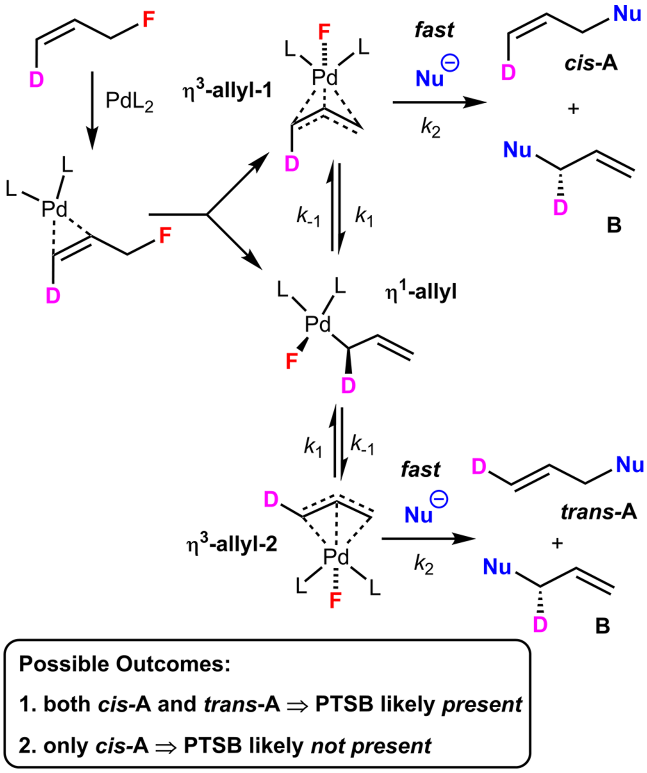

Possible Outcomes:

1. both *cis*-A and *trans*-A ⇒ PTSB likely *present*
2. only *cis*-A ⇒ PTSB likely *not present*

Figure 15. Possible stereochemical labeling probe for verifying the theoretical prediction for the presence of a PTSB.

Here, the nucleophile (Nu) could be a malonate anion or a more reactive nucleophile as needed. Alternatively, the **η^1-allyl** could also be formed initially, as demonstrated to be preferred from MEP analysis. The **η^1-allyl** is normally not susceptible to nucleophilic addition and would thus isomerize to the **η^3-allyl-1** and **η^3-allyl-2** intermediates equally, which would lead to equal amounts of ***cis*-A** and ***trans*-A**. If a PTSB is indeed present, then both the **η^1-allyl** and **η^3-allyl-1** would initially form. The **η^1-allyl** could isomerize to **η^3-allyl-1**, leading to *cis*-**A** and **B**, or it can undergo a fast C−C bond rotation with subsequent reassociation with the π-bond to give **η^3-allyl-2**, which would form the ***trans*-A** product along with **B**.

Therefore, detection of both ***trans*-A** and ***cis*-A** would support the presence of a PTSB, whereas detection of only ***cis*-A** would support the absence of a PTSB.

CONCLUSIONS

The mechanism of the palladium-promoted activation of allylic halides has been investigated using AIMD simulations. The hypothesis for the presence of a PTSB in allylic activation, in which the η^1 and η^3 allyls are both direct products of the bond activation and share a TS, has been supported by analysis of the MEP and MD simulations initiated at the TS. The dynamics predicts that allylic chloride activation promoted by palladium favors formation of the η^3 allyl in both the gas and solution phases, with bifurcation being present albeit in minor amounts. In contrast, allylic fluoride activation is predicted to favor formation of the η^1 allyl in the gas phase and at low dielectrics ($\varepsilon < 2.6$) with a switch in preference to the η^3 allyl in higher dielectrics, using a trialkylphosphine ligand. The MEP preference agrees with the product preference predicted by the dynamics predictions. These results counter the traditional assumption that the singular direct product of activation is the η^3 allyl, and that η^1 is only accessed from η^3 via $\sigma \leftrightarrow \pi$ isomerization.

The stereochemical course of allylic substitution reactions has a complex dependence on the nature of the η^1 and η^3 relative populations and their interconversion. The results of this study suggest that η^1 and η^3 are both formed directly, without the need for a thermodynamic equilibrium to be reached. Under kinetic control, both η^1 and η^3 are predicted to form, which may have substantial implications for the stereochemical outcome of allylic substitution reactions. These findings challenge the current understanding of the mechanism of transition-metal-catalyzed allylic substitution, as well as other organometallic processes involving the intermediacy of π-allyl intermediates. These conclusions merit further investigations into the general applicability to other allylic systems as well as toward the experimental verification thereof.

ASSOCIATED CONTENT

Supporting Information

The Supporting Information is available free of charge at https://pubs.acs.org/doi/10.1021/acs.joc.1c00891.

Additional dynamics results, reaction energy profiles, IRCs, and coordinates (PDF)

AUTHOR INFORMATION

Corresponding Author

Lawrence M. Wolf − *Department of Chemistry, Kennedy College of Sciences, University of Massachusetts Lowell, Lowell, Massachusetts 01854, United States*; orcid.org/0000-0002-8035-4137; Email: Lawrence_Wolf@uml.edu

Author

Malkaye Kpante − *Department of Chemistry, Kennedy College of Sciences, University of Massachusetts Lowell, Lowell, Massachusetts 01854, United States*

Complete contact information is available at:
https://pubs.acs.org/10.1021/acs.joc.1c00891

Funding

The authors are grateful for the financial support from the National Science Foundation (CHE-1808671).

Notes

The authors declare no competing financial interest.

ACKNOWLEDGMENTS

We acknowledge the National Science Foundation for partial support of this research (CHE-1808671). We also gratefully acknowledge the University of Massachusetts Green High Performance Computing Cluster (MGHPCC) for access to supercomputing resources.

REFERENCES

(1) Trost, B. M.; Van Vranken, D. L. Asymmetric Transition Metal-Catalyzed Allylic Alkylations. *Chem. Rev.* **1996**, *96*, 395−422.

(2) Trost, B. M.; Crawley, M. L. Asymmetric Transition-Metal-Catalyzed Allylic Alkylations: Applications in Total Synthesis. *Chem. Rev.* **2003**, *103*, 2921−2944.

(3) Trost, B. M. Asymmetric Allylic Alkylation, an Enabling Methodology. *J. Org. Chem.* **2004**, *69*, 5813−5837.

(4) Lu, Z.; Ma, S. Metal-Catalyzed Enantioselective Allylation in Asymmetric Synthesis. *Angew. Chem., Int. Ed.* **2008**, *47*, 258−297.

(5) Ess, D. H.; Wheeler, S. E.; Iafe, R. G.; Xu, L.; Celebi-Olcum, N.; Houk, K. N. Bifurcations on potential energy surfaces of organic reactions. *Angew. Chem., Int. Ed.* **2008**, *47*, 7592−7601.

(6) Cheng, Q.; Tu, H. F.; Zheng, C.; Qu, J. P.; Helmchen, G.; You, S. L. Iridium-Catalyzed Asymmetric Allylic Substitution Reactions. *Chem. Rev.* **2019**, *119*, 1855−1969.

(7) Biswas, S.; Huang, Z.; Choliy, Y.; Wang, D. Y.; Brookhart, M.; Krogh-Jespersen, K.; Goldman, A. S. Olefin isomerization by iridium pincer catalysts. Experimental evidence for an eta3-allyl pathway and an unconventional mechanism predicted by DFT calculations. *J. Am. Chem. Soc.* **2012**, *134*, 13276−13295.

(8) Hu, L.; Wu, Z.; Huang, G. Mechanism and Origins of Regio- and Stereoselectivities in Iridium-Catalyzed Isomerization of 1-Alkenes to trans-2-Alkenes. *Org. Lett.* **2018**, *20*, 5410−5413.

(9) Xue, X. S.; Ji, P.; Zhou, B.; Cheng, J. P. The Essential Role of Bond Energetics in C-H Activation/Functionalization. *Chem. Rev.* **2017**, *117*, 8622−8648.

(10) Consiglio, G.; Waymouth, R. M. Enantioselective homogeneous catalysis involving transition-metal-allyl intermediates. *Chem. Rev.* **1989**, *89*, 257−276.

(11) Kurosawa, H.; Ogoshi, S.; Kawasaki, Y.; Murai, S.; Miyoshi, M.; Ikeda, I. Novel dependency of stereochemistry upon metal, ligand, and solvent in oxidative addition of allylic chloride to palladium(0) and platinum(0) complexes. *J. Am. Chem. Soc.* **1990**, *112*, 2813−2814.

(12) Kurosawa, H.; Kajimaru, H.; Ogoshi, S.; Yoneda, H.; Miki, K.; Kasai, N.; Murai, S.; Ikeda, I. Novel syn oxidative addition of allylic halides to olefin complexes of palladium(0) and platinum(0). *J. Am. Chem. Soc.* **1992**, *114*, 8417−8424.

(13) Wolf, L. M.; Thiel, W. Origin of inversion versus retention in the oxidative addition of 3-chloro-cyclopentene to Pd(0)L(n). *J. Org. Chem.* **2014**, *79*, 12136−12147.

(14) Eyring, H. The Activated Complex in Chemical Reactions. *J. Chem. Phys.* **1935**, *3*, 107−115.

(15) Wigner, E. The transition state method. *Trans. Faraday Soc* **1938**, *34*, 29−41.

(16) Hare, S. R.; Tantillo, D. J. Post-transition state bifurcations gain momentum − current state of the field. *Pure Appl. Chem.* **2017**, *89*, 679−698.

(17) Caramella, P.; Quadrelli, P.; Toma, L. An Unexpected Bispericyclic Transition Structure Leading to 4+2 and 2+4 Cycloadducts in the Endo Dimerization of Cyclopentadiene. *J. Am. Chem. Soc.* **2002**, *124*, 1130−1131.

(18) Quadrelli, P.; Romano, S.; Toma, L.; Caramella, P. Merging and bifurcation of 4+2 and 2+4 cycloaddition modes in the archetypal

dimerization of butadiene. A case of competing bispericyclic, pericyclic and diradical paths. *Tetrahedron Lett.* **2002**, *43*, 8785−8789.

(19) Quadrelli, P.; Romano, S.; Toma, L.; Caramella, P. A Bispericyclic Transition Structure Allows for Efficient Relief of Antiaromaticity Enhancing Reactivity and Endo Stereoselectivity in the Dimerization of the Fleeting Cyclopentadienone. *J. Org. Chem.* **2003**, *68*, 6035−6038.

(20) Leach, A. G.; Goldstein, E.; Houk, K. N. A Cornucopia of Cycloadducts: Theoretical Predictions of the Mechanisms and Products of the Reactions of Cyclopentadiene with Cycloheptatriene. *J. Am. Chem. Soc.* **2003**, *125*, 8330−8339.

(21) Limanto, J.; Khuong, K. S.; Houk, K. N.; Snapper, M. L. Intramolecular Cycloadditions of Cyclobutadiene with Dienes: Experimental and Computational Studies of the Competing (2 + 2) and (4 + 2) Modes of Reaction. *J. Am. Chem. Soc.* **2003**, *125*, 16310−16321.

(22) Singleton, D. A.; Hang, C.; Szymanski, M. J.; Meyer, M. P.; Leach, A. G.; Kuwata, K. T.; Chen, J. S.; Greer, A.; Foote, C. S.; Houk, K. N. Mechanism of Ene Reactions of Singlet Oxygen. A Two-Step No-Intermediate Mechanism. *J. Am. Chem. Soc.* **2003**, *125*, 1319−1328.

(23) Ussing, B. R.; Hang, C.; Singleton, D. A. Dynamic Effects on the Periselectivity, Rate, Isotope Effects, and Mechanism of Cycloadditions of Ketenes with Cyclopentadiene. *J. Am. Chem. Soc.* **2006**, *128*, 7594−7607.

(24) Bekele, T.; Christian, C. F.; Lipton, M. A.; Singleton, D. A. “Concerted” Transition State, Stepwise Mechanism. Dynamics Effects in C2-C6 Enyne Allene Cyclizations. *J. Am. Chem. Soc.* **2005**, *127*, 9216−9223.

(25) Çelebi-Ölçüm, N.; Ess, D. H.; Aviyente, V.; Houk, K. N. Lewis Acid Catalysis Alters the Shapes and Products of Bis-Pericyclic Diels−Alder Transition States. *J. Am. Chem. Soc.* **2007**, *129*, 4528−4529.

(26) Thomas, J. B.; Waas, J. R.; Harmata, M.; Singleton, D. A. Control Elements in Dynamically Determined Selectivity on a Bifurcating Surface. *J. Am. Chem. Soc.* **2008**, *130*, 14544−14555.

(27) Çelebi-Ölçüm, N.; Ess, D. H.; Aviyente, V.; Houk, K. N. Effect of Lewis Acid Catalysts on Diels−Alder and Hetero-Diels−Alder Cycloadditions Sharing a Common Transition State. *J. Org. Chem.* **2008**, *73*, 7472−7480.

(28) Wang, Z.; Hirschi, J. S.; Singleton, D. A. Recrossing and Dynamic Matching Effects on Selectivity in a Diels−Alder Reaction. *Angew. Chem., Int. Ed.* **2009**, *48*, 9156−9159.

(29) Pham, H. V.; Houk, K. N. Diels-Alder reactions of allene with benzene and butadiene: concerted, stepwise, and ambimodal transition states. *J. Org. Chem.* **2014**, *79*, 8968−8976.

(30) Yu, P.; Patel, A.; Houk, K. N. Transannular [6 + 4] and Ambimodal Cycloaddition in the Biosynthesis of Heronamide A. *J. Am. Chem. Soc.* **2015**, *137*, 13518−13523.

(31) Patel, A.; Chen, Z.; Yang, Z.; Gutiérrez, O.; Liu, H.-W.; Houk, K. N.; Singleton, D. A. Dynamically Complex [6+4] and [4+2] Cycloadditions in the Biosynthesis of Spinosyn A. *J. Am. Chem. Soc.* **2016**, *138*, 3631−3634.

(32) Yu, P.; Chen, T. Q.; Yang, Z.; He, C. Q.; Patel, A.; Lam, Y. H.; Liu, C. Y.; Houk, K. N. Mechanisms and Origins of Periselectivity of the Ambimodal [6 + 4] Cycloadditions of Tropone to Dimethylfulvene. *J. Am. Chem. Soc.* **2017**, *139*, 8251−8258.

(33) Villar López, R.; Faza, O. N.; Silva López, C. Silva Lopez, C., Dynamic Effects Responsible for High Selectivity in a [3,3] Sigmatropic Rearrangement Featuring a Bispericyclic Transition State. *J. Org. Chem.* **2017**, *82*, 4758−4765.

(34) Burns, J. M. Computational evidence for a reaction pathway bifurcation in Sasaki-type (4 + 3)-cycloadditions. *Org. Biomol. Chem.* **2018**, *16*, 1828−1836.

(35) Chen, S.; Yu, P.; Houk, K. N. Ambimodal Dipolar/Diels-Alder Cycloaddition Transition States Involving Proton Transfers. *J. Am. Chem. Soc.* **2018**, *140*, 18124−18131.

(36) Yang, Z.; Dong, X.; Yu, Y.; Yu, P.; Li, Y.; Jamieson, C.; Houk, K. N. Relationships between Product Ratios in Ambimodal Pericyclic Reactions and Bond Lengths in Transition Structures. *J. Am. Chem. Soc.* **2018**, *140*, 3061−3067.

(37) Yang, Z.; Yang, S.; Yu, P.; Li, Y.; Doubleday, C.; Park, J.; Patel, A.; Jeon, B. S.; Russell, W. K.; Liu, H. W.; Russell, D. H.; Houk, K. N. Influence of water and enzyme SpnF on the dynamics and energetics of the ambimodal [6+4]/[4+2] cycloaddition. *Proc. Natl. Acad. Sci. U.S.A.* **2018**, *115*, E848−E855.

(38) Yang, Z.; Zou, L.; Yu, Y.; Liu, F.; Dong, X.; Houk, K. N. Molecular dynamics of the two-stage mechanism of cyclopentadiene dimerization: concerted or stepwise? *Chem. Phys.* **2018**, *514*, 120−125.

(39) Hare, S. R.; Li, A.; Tantillo, D. J. Post-transition state bifurcations induce dynamical detours in Pummerer-like reactions. *Chem. Sci.* **2018**, *9*, 8937−8945.

(40) Xue, X. S.; Jamieson, C. S.; Garcia-Borras, M.; Dong, X.; Yang, Z.; Houk, K. N. Ambimodal Trispericyclic Transition State and Dynamic Control of Periselectivity. *J. Am. Chem. Soc.* **2019**, *141*, 1217−1221.

(41) Burns, J. M.; Boittier, E. D. Pathway Bifurcation in the (4 + 3)/(5 + 2)-Cycloaddition of Butadiene and Oxidopyrylium Ylides: The Significance of Molecular Orbital Isosymmetry. *J. Org. Chem.* **2019**, *84*, 5997−6005.

(42) Campos, R. B.; Tantillo, D. J. Designing Reactions with Post-Transition-State Bifurcations: Asynchronous Nitrene Insertions into C−C σ Bonds. *Chem* **2019**, *5*, 227−236.

(43) Garayalde, D.; Gómez-Bengoa, E.; Huang, X.; Goeke, A.; Nevado, C. Mechanistic Insights in Gold-Stabilized Nonclassical Carbocations: Gold-Catalyzed Rearrangement of 3-Cyclopropyl Propargylic Acetates. *J. Am. Chem. Soc.* **2010**, *132*, 4720−4730.

(44) Wang, Z. J.; Benitez, D.; Tkatchouk, E.; Goddard III, W. A.; Toste, F. D. Mechanistic Study of Gold(I)-Catalyzed Intermolecular Hydroamination of Allenes. *J. Am. Chem. Soc.* **2010**, *132*, 13064−13071.

(45) Noey, E. L.; Wang, X.; Houk, K. N. Selective gold(I)-catalyzed formation of tetracyclic indolines: a single transition structure and bifurcations lead to multiple products. *J. Org. Chem.* **2011**, *76*, 3477−3483.

(46) Hansen, J. H.; Gregg, T. M.; Ovalles, S. R.; Lian, Y.; Autschbach, J.; Davies, H. M. L. On the Mechanism and Selectivity of the Combined C−H Activation/Cope Rearrangement. *J. Am. Chem. Soc.* **2011**, *133*, 5076−5085.

(47) Ye, L.; Wang, Y.; Aue, D. H.; Zhang, L. Experimental and Computational Evidence for Gold Vinylidenes: Generation from Terminal Alkynes via a Bifurcation Pathway and Facile C−H Insertions. *J. Am. Chem. Soc.* **2012**, *134*, 31−34.

(48) Hashmi, A. S. K.; Wieteck, M.; Braun, I.; Rudolph, M.; Rominger, F. Gold Vinylidene Complexes: Intermolecular C(sp3) H Insertions and Cyclopropanations Pathways. *Angew. Chem., Int. Ed.* **2012**, *51*, 10633−10637.

(49) Wang, Y.; Yepremyan, A.; Ghorai, S.; Todd, R.; Aue, D. H.; Zhang, L. Gold-Catalyzed Cyclizations of cis-Enediynes: Insights into the Nature of Gold−Aryne Interactions. *Angew. Chem., Int. Ed.* **2013**, *52*, 7795−7799.

(50) Vilhelmsen, M. H.; Hashmi, A. S. K. Reaction Mechanism for the Dual Gold-Catalyzed Synthesis of Dibenzopentalene: A DFT Study. *Chem. - Eur. J.* **2014**, *20*, 1901−1908.

(51) Hansmann, M. M.; Tšupova, S.; Rudolph, M.; Rominger, F.; Hashmi, A. S. K. Gold-Catalyzed Cyclization of Diynes: Controlling the Mode of 5-endo versus 6-endo Cyclization—An Experimental and Theoretical Study by Utilizing Diethynylthiophenes. *Chem.−Eur. J.* **2014**, *20*, 2215−2223.

(52) Zhang, L.; Wang, Y.; Yao, Z.-J.; Wang, S.; Yu, Z.-X. Kinetic or Dynamic Control on a Bifurcating Potential Energy Surface? An Experimental and DFT Study of Gold-Catalyzed Ring Expansion and Spirocyclization of 2-Propargyl-β-tetrahydrocarbolines. *J. Am. Chem. Soc.* **2015**, *137*, 13290−13300.

(53) Hare, S. R.; Tantillo, D. J. Cryptic post-transition state bifurcations that reduce the efficiency of lactone-forming Rh-carbenoid C-H insertions. *Chem. Sci.* **2017**, *8*, 1442−1449.

(54) Zhang, Y.; Karunananda, M. K.; Yu, H.-C.; Clark, K. J.; Williams, W.; Mankad, N. P.; Ess, D. H. Dynamically Bifurcating Hydride Transfer Mechanism and Origin of Inverse Isotope Effect for Heterodinuclear AgRu-Catalyzed Alkyne Semihydrogenation. *ACS Catal.* **2019**, *9*, 2657−2663.

(55) Carlsen, R.; Jenkins, J. R.; Ess, D. H. Direct dynamics analysis of the cationic Cp*(PMe3)Ir(CH3) methane C−H activation mechanism. *Faraday Discuss.* **2019**, *220*, 414−424.

(56) Carlsen, R.; Jenkins, J. R.; Huang, T.-C. J.; Pugh, S. L.; Ess, D. H. Paddle Ball Dynamics during Conversion of a Rh−Methyl Hydride Complex to a Rh−Methane σ-Complex through Reductive Coupling. *Organometallics* **2019**, *38*, 2280−2287.

(57) Smith, J. A.; Schouten, A.; Wilde, J. H.; Westendorff, K. S.; Dickie, D. A.; Ess, D. H.; Harman, W. D. Experiments and Direct Dynamics Simulations That Probe η2-Arene/Aryl Hydride Equilibria of Tungsten Benzene Complexes. *J. Am. Chem. Soc.* **2020**, *142*, 16437−16454.

(58) Teynor, M. S.; Carlsen, R.; Ess, D. H. Relationship Between Energy Landscape Shape and Dynamics Trajectory Outcomes for Methane C−H Activation by Cationic Cp*(PMe3)Ir/Rh/Co(CH3). *Organometallics* **2020**, *39*, 1393−1403.

(59) Wheeler, J. I.; Carlsen, R.; Ess, D. H. Mechanistic molecular motion of transition-metal mediated β-hydrogen transfer: quasiclassical trajectories reveal dynamically ballistic, dynamically unrelaxed, two step, and concerted mechanisms. *Dalton Trans.* **2020**, *49*, 7747−7757.

(60) Carlsen, R.; Maley, S. M.; Ess, D. H. Timing and Structures of σ-Bond Metathesis C−H Activation Reactions from Quasiclassical Direct Dynamics Simulations. *Organometallics* **2021**, *40*, 1454−1465.

(61) Zheng, C. Divergent Pathways and Dynamic Effects of Intramolecular Hydride Transfer Reactions Mediated by Cp*M(III) Complexes (M = Co, Rh, Ir)†. *Chin. J. Chem.* **2020**, *38*, 1579−1584.

(62) Lee, S.; Goodman, J. M. Rapid Route-Finding for Bifurcating Organic Reactions. *J. Am. Chem. Soc.* **2020**, *142*, 9210−9219.

(63) Ito, T.; Harabuchi, Y.; Maeda, S. AFIR explorations of transition states of extended unsaturated systems: automatic location of ambimodal transition states. *Phys. Chem. Chem. Phys.* **2020**, *22*, 13942−13950.

(64) Hazari, A.; Gouverneur, V.; Brown, J. M. Palladium-catalyzed substitution of allylic fluorides. *Angew. Chem., Int. Ed.* **2009**, *48*, 1296−1299.

(65) Benedetto, E.; Keita, M.; Tredwell, M.; Hollingworth, C.; Brown, J. M.; Gouverneur, V. Platinum-Catalyzed Substitution of Allylic Fluorides. *Organometallics* **2012**, *31*, 1408−1416.

(66) Zhang, H.; Lin, J.-H.; Xiao, J.-C.; Gu, Y.-C. Rh-catalyzed allylic C−F bond activation: the stereoselective synthesis of trisubstituted monofluoroalkenes and a mechanism study. *Org. Biomol. Chem.* **2014**, *12*, 581−588.

(67) Ichitsuka, T.; Fujita, T.; Ichikawa, J. Nickel-Catalyzed Allylic C(sp3)−F Bond Activation of Trifluoromethyl Groups via β-Fluorine Elimination: Synthesis of Difluoro-1,4-dienes. *ACS Catal.* **2015**, *5*, 5947−5950.

(68) Shen, Q.; Huang, Y.-G.; Liu, C.; Xiao, J.-C.; Chen, Q.-Y.; Guo, Y. Review of recent advances in CF bond activation of aliphatic fluorides. *J. Fluorine Chem.* **2015**, *179*, 14−22.

(69) Unzner, T. A.; Magauer, T. Carbon−fluorine bond activation for the synthesis of functionalized molecules. *Tetrahedron Lett.* **2015**, *56*, 877−883.

(70) Zhang, X.; Liu, Y.; Chen, G.; Pei, G.; Bi, S. Theoretical Insight into C(sp3)−F Bond Activations and Origins of Chemo- and Regioselectivities of "Tunable" Nickel-Mediated/-Catalyzed Couplings of 2-Trifluoromethyl-1-alkenes with Alkynes. *Organometallics* **2017**, *36*, 3739−3749.

(71) Hamel, J.-D.; Paquin, J.-F. Activation of C−F bonds α to C−C multiple bonds. *Chem. Commun.* **2018**, *54*, 10224−10239.

(72) Trost, B. M.; Gholami, H.; Zell, D. Palladium-Catalyzed Asymmetric Allylic Fluoroalkylation/Trifluoromethylation. *J. Am. Chem. Soc.* **2019**, *141*, 11446−11451.

(73) Butcher, T. W.; Yang, J. L.; Amberg, W. M.; Watkins, N. B.; Wilkinson, N. D.; Hartwig, J. F. Desymmetrization of difluoromethylene groups by C−F bond activation. *Nature* **2020**, *583*, 548−553.

(74) Becke, A. D. Density-functional exchange-energy approximation with correct asymptotic behavior. *Phys. Rev. A* **1988**, *38*, 3098−3100.

(75) Becke, A. D. Density-functional thermochemistry. III. The role of exact exchange. *J. Chem. Phys.* **1993**, *98*, 5648−5652.

(76) Grimme, S.; Antony, J.; Ehrlich, S.; Krieg, H. A consistent and accurate ab initio parametrization of density functional dispersion correction (DFT-D) for the 94 elements H-Pu. *J. Chem. Phys.* **2010**, *132*, No. 154104.

(77) Steinmetz, M.; Grimme, S. Benchmark Study of the Performance of Density Functional Theory for Bond Activations with (Ni,Pd)-Based Transition-Metal Catalysts. *ChemistryOpen* **2013**, *2*, 115−124.

(78) Schäfer, A.; Horn, H.; Ahlrichs, R. Fully optimized contracted Gaussian basis sets for atoms Li to Kr. The. *J. Chem. Phys.* **1992**, *97*, 2571−2577.

(79) Weigend, F.; Ahlrichs, R. Balanced basis sets of split valence, triple zeta valence and quadruple zeta valence quality for H to Rn: Design and assessment of accuracy. *Phys. Chem. Chem. Phys.* **2005**, *7*, 3297−3305.

(80) Weigend, F. Accurate Coulomb-fitting basis sets for H to Rn. *Phys. Chem. Chem. Phys.* **2006**, *8*, 1057−1065.

(81) Eichkorn, K.; Treutler, O.; Öhm, H.; Häser, M.; Ahlrichs, R. Auxiliary basis sets to approximate Coulomb potentials. *Chem. Phys. Lett.* **1995**, *240*, 283−290.

(82) Eichkorn, K.; Treutler, O.; Öhm, H.; Häser, M.; Ahlrichs, R. Auxiliary basis sets to approximate Coulomb potentials (Chem. Phys. Letters 240 (1995) 283-290). *Chem. Phys. Lett.* **1995**, *242*, 652−660.

(83) Klamt, A.; Schüürmann, G. COSMO: a new approach to dielectric screening in solvents with explicit expressions for the screening energy and its gradient. *J. Chem. Soc., Perkin Trans. 2* **1993**, *2*, 799−805.

(84) Klamt, A. Conductor-like Screening Model for Real Solvents: A New Approach to the Quantitative Calculation of Solvation Phenomena. *J. Phys. Chem. A* **1995**, *99*, 2224−2235.

(85) Perdew, J. P.; Wang, Y. Accurate and simple analytic representation of the electron-gas correlation energy. *Phys. Rev. B* **1992**, *45*, 13244−13249.

(86) Perdew, J. P.; Burke, K.; Ernzerhof, M. Generalized Gradient Approximation Made Simple. *Phys. Rev. Lett.* **1996**, *77*, 3865−3868.

(87) Perdew, J. P.; Ernzerhof, M.; Burke, K. Rationale for mixing exact exchange with density functional approximations. *J. Chem. Phys.* **1996**, *105*, 9982−9985.

(88) Adamo, C.; Barone, V. Toward reliable density functional methods without adjustable parameters: The PBE0 model. *J. Chem. Phys.* **1999**, *110*, 6158−6170.

(89) Zhao, Y.; Truhlar, D. G. The M06 suite of density functionals for main group thermochemistry, thermochemical kinetics, noncovalent interactions, excited states, and transition elements: two new functionals and systematic testing of four M06-class functionals and 12 other functionals. *Theor. Chem. Acc.* **2008**, *120*, 215−241.

(90) Tao, J.; Perdew, J. P.; Staroverov, V. N.; Scuseria, G. E. Climbing the Density Functional Ladder: Nonempirical Meta−Generalized Gradient Approximation Designed for Molecules and Solids. *Phys. Rev. Lett.* **2003**, *91*, No. 146401.

(91) Staroverov, V. N.; Scuseria, G. E.; Tao, J.; Perdew, J. P. Comparative assessment of a new nonempirical density functional: Molecules and hydrogen-bonded complexes. *J. Chem. Phys.* **2003**, *119*, 12129−12137.

(92) Riplinger, C.; Neese, F. An efficient and near linear scaling pair natural orbital based local coupled cluster method. *J. Chem. Phys.* **2013**, *138*, No. 034106.

(93) Riplinger, C.; Sandhoefer, B.; Hansen, A.; Neese, F. Natural triple excitations in local coupled cluster calculations with pair natural orbitals. *J. Chem. Phys.* **2013**, *139*, No. 134101.

(94) Riplinger, C.; Pinski, P.; Becker, U.; Valeev, E. F.; Neese, F. Sparse maps–A systematic infrastructure for reduced-scaling electronic structure methods. II. Linear scaling domain based pair natural orbital coupled cluster theory. *J. Chem. Phys.* **2016**, *144*, No. 024109.
(95) Neese, F. The ORCA program system. *WIREs Comput. Mol. Sci.* **2012**, *2*, 73−78.
(96) Neese, F. Software update: the ORCA program system, version 4.0. *WIREs Comput. Mol. Sci.* **2018**, *8*, No. e1327.
(97) Contreras-García, J.; Johnson, E. R.; Keinan, S.; Chaudret, R.; Piquemal, J.-P.; Beratan, D. N.; Yang, W. NCIPLOT: A Program for Plotting Noncovalent Interaction Regions. *J. Chem. Theory Comput.* **2011**, *7*, 625−632.
(98) Zhang, Z.; Jamieson, C. S.; Zhao, Y. L.; Li, D.; Ohashi, M.; Houk, K. N.; Tang, Y. Enzyme-Catalyzed Inverse-Electron Demand Diels-Alder Reaction in the Biosynthesis of Antifungal Ilicicolin H. *J. Am. Chem. Soc.* **2019**, *141*, 5659−5663.
(99) Ahlrichs, R.; Bär, M.; Häser, M.; Horn, H.; Kölmel, C. Electronic structure calculations on workstation computers: The program system turbomole. *Chem. Phys. Lett.* **1989**, *162*, 165−169.
(100) Yamamoto, Y.; Hasegawa, H.; Yamataka, H. Dynamic path bifurcation in the Beckmann reaction: support from kinetic analyses. *J. Org. Chem.* **2011**, *76*, 4652−4660.

https://doi.org/10.1021/acs.joc.1c00891